IEEE Access
Multidisciplinary | Rapid Review | Open Access Journal

Received December 16, 2019, accepted December 19, 2019, date of publication December 25, 2019,
date of current version January 3, 2020.

Digital Object Identifier 10.1109/ACCESS.2019.2961761

Capacitive Sensing and Electrostatic Control System Design and Analysis With a Torsion Pendulum

YUKUN WANG, KEQI QI, SHAOXIN WANG, WEI LI, ZHE LI, AND ZHI WANG
State Key Laboratory of Applied Optics, Changchun Institute of Optics, Fine Mechanics and Physics, Chinese Academy of Sciences, Changchun 130033, China

Corresponding authors: Shaoxin Wang (wangshaoxin@ciomp.ac.cn) and Zhi Wang (wz070611@126.com)

This work was supported in part by the Strategic Priority Research Program of the Chinese Academy of Science under Grant XDA15020704.

ABSTRACT The micro capacitive sensing and electrostatic drive control system (front-end electronics, FEE) is the core component of inertial sensor in space gravitational wave detection. The FEE requires high-precision displacement detection, high-stability electrostatic drive, and stable system control to achieve an acceleration resolution of 10^{-15} m/s^2/Hz$^{1/2}$ in the low-frequency range of 0.1 mHz-1 Hz. Based on the requirements of the future Chinese space gravitational wave detection task (Taiji Program), this paper conducted key technical research of the FEE using differential capacitance detections and electrostatic drives. The structure and working principle of the FEE were also introduced. The structural parameters of the entire system, working parameters, and electrostatic control system model were provided, and the performance of the PID controller was analyzed. Finally, using the torsion pendulum to overcome the influence of gravity on the earth, the FEE multi-degree of freedom control function was verified on the vibration isolation marble platform, the measurement range and power conversion coefficient were calibrated, and the noise level under current conditions was measured. Experimental results show that the FEE developed in this paper can achieve stable control in multiple degrees of freedom, the acceleration range is larger than 10^{-3} m/s^2, the electric force conversion factor is 4.8×10^{-3} m/s^2/V, and the measured acceleration resolution is 9.6×10^{-6} m/s^2/Hz$^{1/2}$. After optimizing the sensitive structure parameters, the acceleration resolution can be estimated at 3.3×10^{-15} m/s^2/Hz$^{1/2}$. These results satisfy the Taiji Program requirements. This paper provides a solid foundation for the future exploration of space gravitational waves in China and clears the optimization direction for the next step.

INDEX TERMS Gravitational wave detection, Chinese Taiji Program, inertial sensor, capacitive sensing and electrostatic drive control system, torsion pendulum.

I. INTRODUCTION

In February 2016, the American Laser Interferometer Gravitational-Wave Observatory (LIGO) directly detected gravitational wave, which confirmed the prediction of Einstein regarding the existence of gravitational waves a century ago and created gravitational wave astronomy [1]. In August 2017, LIGO of the United States and Virgo of Italy first discovered a double neutron star combined with the gravitational wave event and found the electromagnetic counterpart of the gravitational wave event [2]. This detection of gravitational waves and electromagnetic counterparts has epoch-making importance in the history of astronomy and physics, which officially opened the era of gravitational wave astronomy. Ground gravitational wave measurement is affected by the gravity of the Earth and the scale size. The range of detected gravitational waves is mainly concentrated in the mid-high frequency of 10 Hz to 10 kHz. However, gravitational wave information is abundant in the low-frequency range of 0.1 mHz to 1 Hz. Space gravitational wave detection is the only option for studying gravitational waves and the nature of wave sources in a wide frequency range.

Space gravitational wave detection uses an ultra-high-precision interferometric measurement system to measure the

The associate editor coordinating the review of this manuscript and approving it for publication was Derek Abbott.

TABLE 1. Measurement range, resolution, and bandwidth of electrostatic accelerometers abroad.

Model	Axis	Acceleration		Bandwidth(Hz)
		Range(g_0)	Resolution(g_0)	
MESA	x	$(-1-1)\times10^{-4}$	3.05^{-9}	1×10^{-4}-1
	y,z	$(-1.5-1.5)\times10^{-4}$	4.6^{-9}	1×10^{-4}-1
ASTRE	x	$(-1.32-1.32)\times10^{-4}$	1^{-8}	DC-1.9
	yz	$(-1.36-1.36)\times10^{-4}$	1^{-9}	DC-1.9
STAR	x	$(-1-1)\times10^{-5}$	3.05^{-9}	$1\times10^{-4}-1\times10^{-1}$
	yz	$(-1-1)\times10^{-5}$	3.05^{-9}	$1\times10^{-4}-1\times10^{-1}$
GRADIO	x	$(-3.05-3.05)\times10^{-5}$	3.05^{-11}	0.005-0.125
	yz	$(-2.55-2.55)\times10^{-6}$	5.1^{-13}	0.005-0.125

distance change between the two test masses (TM) with the picometer precision, thereby obtaining the gravitational wave signal. The inertial sensor is one of the most important parts of space gravitational wave detection device. The main function of this sensor is to release the TM into space freely and realize drag-free control. Simultaneously, electrostatic force control is used to ensure the maximum movement of TM along the geodesic; that is, the noise applied to the TM is as small as possible. Therefore, the performance of the inertial sensor directly affects the accuracy and even the success or failure of space gravitational wave detection system.

The resolution of the inertial sensor must reach 10^{-15} m/s^2/Hz$^{1/2}$ to realize the detection of space gravitational waves. To date, the United States and Europe have used the electrostatic suspension accelerometer to launch MESA, ASTRE, STAR, GRADIO, and other accelerometers, and the highest measurement resolution has reached 10^{-13} m/s^2/Hz$^{1/2}$ [3]–[6], as shown in Table 1. Internationally, the earliest project to develop space gravitational wave detection was the collaborative space laser interference antenna LISA (laser interferometer space antenna) project of NASA and the European Space Agency (ESA) in the 1990s [7]. In December 2015, the LISA pathfinder was launched to demonstrate and test LISA-related technology, and the resolution reached the order of 10^{-15} m/s^2 [8]. As a representative of space gravitational wave detection project, LISA has drawn a clear path and platform for space gravitational wave detection discipline at the level of mission concept.

The Huazhong University of Science and Technology in China has researched on electrostatic suspension accelerometers since 2000 [9]–[11], and the resolution by high-pressure suspension test has reached 4×10^{-8} m/s^2/Hz$^{1/2}$. The test level of the torsion pendulum suspension is better than 10^{-11} m/s^2/Hz$^{1/2}$. In 2013, a scientific experimental satellite was installed to complete function verification, but the acceleration resolution test level was not provided. The Lanzhou Institute of Physics has also conducted considerable work in this field [12], [13] and achieved important results in key technology research, ground performance testing, development process, and prototype engineering. The ground test accuracy of high-voltage suspension accelerometer reached 10^{-9} m/s^2/Hz$^{1/2}$. In 2008, led by the Institute of Mechanics of the Chinese Academy of Sciences, numerous domestic units set up space gravitational wave detection and demonstration group and conducted substantial research work with the support of the pilot science and technology special space science pre-research project of the Chinese Academy of Sciences. Scientific goals, development routes, program planning, and key technical breakthroughs were proposed, and the Space Taiji Program was introduced in early 2016 [14], [15]. According to the plan, China will launch a gravitational wave detection satellite group around 2030 to conduct direct detection of gravitational waves in the middle and low-frequency bands.

Numerous key technical tasks must be conducted because the technical indicators required for the Taiji Program are much higher than those of the current state of the technology. Based on the requirements of the future Chinese space gravitational wave detection mission (Taiji Program), this paper performs the key technical research of inertial sensor front-end electronics (FEE) and designs a three-degree-of-freedom capacitive sensing and electrostatic drive control system. Furthermore, the influence of gravity is overcome by a torsion pendulum on the ground, and the three-degree-of-freedom stability control is realized. The ground-based measured acceleration resolution index reaches 10^{-7} m/s^2/Hz$^{1/2}$, and the index can reach 10^{-8} m/s^2/Hz$^{1/2}$ after evaluation based on noise analysis. The indicators show that the gravitational wave detection requirements have not yet been reached. However, through the advancement of this prototype, a considerable amount of experimental data and engineering experience has been accumulated for the development of inertial sensor FEE. This study provides optimization direction and design ideas for future FEE research.

The content of this paper is as follows. The second section mainly introduces the composition and basic working principle of the inertial sensor. The third section provides the detailed design of the FEE and the theoretical derivation of the control system. The fourth section gives the ground experimental device and the actual measurement and evaluation results. The final section provides a comprehensive summary of the work in this paper.

II. STRUCTURE AND WORKING PRINCIPLE

The inertial sensor comprises of two units: sensor and FEE. The sensor is used to sense the external interference acceleration signal and convert this signal into a differential capacitance displacement signal output to the FEE unit. The FEE

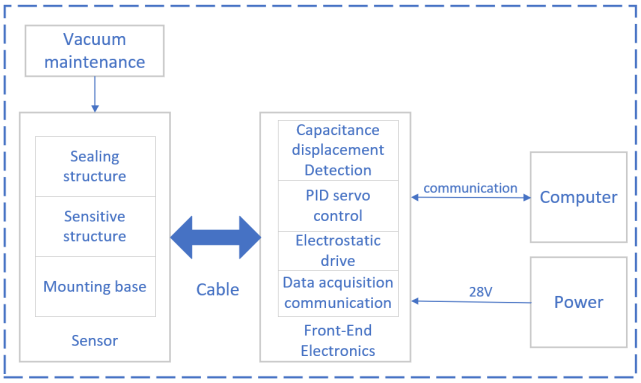

FIGURE 1. Diagram of the inertial sensor composition.

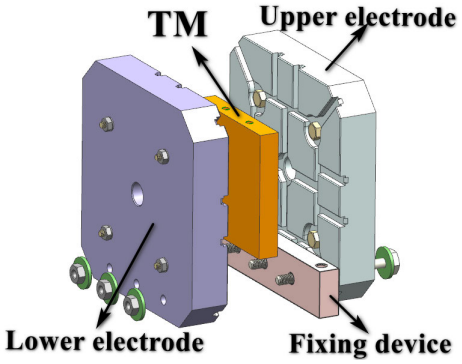

FIGURE 2. Sensitive structure.

is to measure the differential capacitance displacement and calculate the driving voltage for electrosstatic control. Simultaneously, the vacuum device is used for sealing to reduce the gas motion noise. Figure 1 shows the block diagram of the inertial sensor composition.

Figure 1 shows that the sensor mainly comprises of a sealing structure, a sensitive structure, and a mounting base. The sealing structure is used to maintain a vacuum environment and reduce gas molecular perturbations. The sensitive structure comprises of the upper and lower electrodes and the TM, as shown in Figure 2. The sealing and sensitive structures are assembled and mounted on the mounting base.

The sensitive structure of the accelerometer must be installed on the Invar base which has been finely machined to ensure accurate detection of line and angular acceleration. The pedestal has a verticality and parallelism tolerance of 5×10^{-5} rad (equivalent to 10''). In terms of calibration and ground measurement, overcoming the earth's gravity by using the suspension wire torsion pendulum is necessary. The accelerometer core also needs a high vacuum seal to reduce the noise, and its appearance is shown in Figure 3.

The FEE is mainly used to detect the differential capacitance signal input by the sensor and output the corresponding servo feedback voltage signal to the sensor. Thus, the TM is maintained at the center of the sensitive structure, realizing the measurement of the acceleration signal. The working

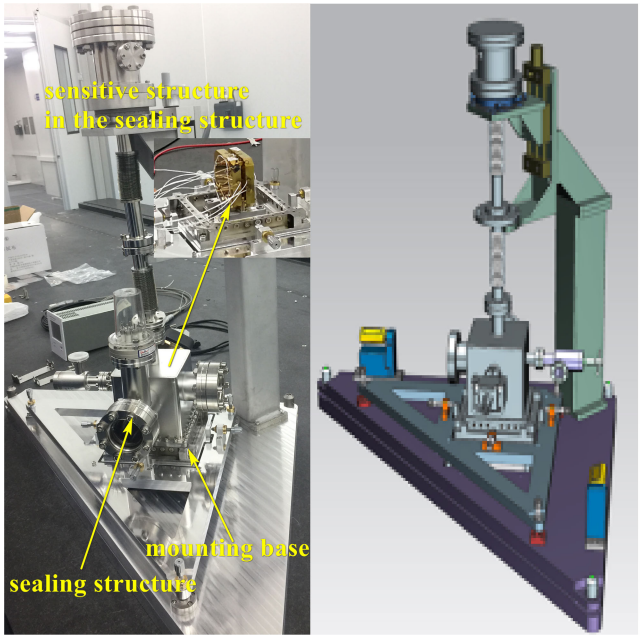

FIGURE 3. Appearance of the sensor structure with a vacuum sealing system.

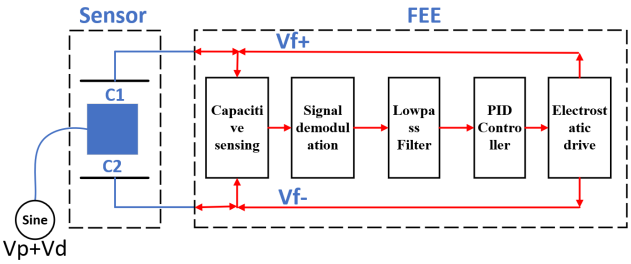

FIGURE 4. Working principle of inertial sensor.

principle is shown in Figure 4. V_d is the injection voltage signal used for differential capacitance detection. V_p is the preload voltage for the electrostatic drive. V_d and V_p are applied to the TM through a gold wire. When an external interference force acts on the TM, the TM will deviate from the center of the electrodes. This phenomenon will result in a change in capacitance C_1 and C_2. C_1 is the capacitance between the TM and the upper electrode, while C_2 is the capacitance between the TM and the lower electrode. The differential capacitance signal C_1-C_2 is detected by the capacitive sensing circuit in FEE. After signal demodulation and low-pass filter modules, the differential capacitance signal finally enters the PID controller module. The feedback voltage signal V_f is then applied to the electrodes through the electrostatic drive circuit, V_f is calculated by the PID controller module, and the TM is pulled back to the center of the electrodes by the electrostatic force. This feedback voltage reflects the magnitude of the external interference acceleration.

When the TM is stably controlled at the center of the electrodes, the feedback control output and the external

TABLE 2. Structure parameters of sensitive structure.

Parameters	Value	Unit
Mass m	70	g
Size of the TM	40 × 40 × 40	mm
Electrode distance of X-axis dx	120	μm
Limit height of X-axis h	70	μm
Electrode area of X1-axis	500	mm^2
Electrode area of X2- and X3-axes	250	mm^2

interference acceleration satisfy the following relationship:

$$a_{\text{out}} = a_e \cong \frac{2\varepsilon_0\varepsilon_r S}{md^2} V_p V_f \tag{1}$$

where ε_0 is the vacuum dielectric constant, ε_r is the relative dielectric constant, S is the electrode area, d is the average electrode distance, V_f is the feedback control voltage, and V_p is the preload voltage applied to the TM.

III. DESIGN OF SENSITIVE STRUCTURE

The TM adopts a flat cube structure. Based on the working principle of the inertial sensor and the measurement output equation and technical specifications, the basic parameters of the sensitive structure of the inertial sensor are shown in Table 2.

The TM material is titanium alloy with a low magnetic susceptibility (less than 2×10^{-4} IU) to reduce the acceleration noise of the inertial sensor. The unevenness of the hexahedron is less than 1 μm. The perpendicularity and parallelism of each face of the TM are less than 10^{-5} rad (equivalent to 2'') to ensure that the three sensitive axes are independent of each other. The differential capacitance formed by the upper and lower electrodes is a sensitive axis. One TM corresponds to three electrode pairs. Thus three sensitive axes can realize three degrees of freedom acceleration measurement.

Figure 5 shows the configuration of the electrodes used to test the TM position and attitude. The electrode material is fused silica with a low-expansion coefficient (5.5×10^{-7}/°C), and the electrode surface is plated with gold film. The electrode unevenness is less than 1 μm, and the area error of each electrode is less than 0.2%. Each electrode surface is divided into four blocks, two of which are connected together and defined as X1. The two other electrodes are defined as X2 and X3.

The three sensitive axes are X1, X2 and X3. These axes can realize one translation and two rotation measurements. Figure 6 shows the measurement principle.

As shown in Figure 6, the translational displacement X and rotational angle θ can be calculated by the following equation:

$$\begin{cases} X = \frac{X_R + X_L}{2} \\ \theta = \arctan\left(\frac{X_R - X_L}{2L}\right) \end{cases} \tag{2}$$

where X_L is the offset from the center of the left electrode pair, X_R is the offset from the center of the right electrode pair, L is the distance from the center of the electrode to the TM central axis, and d is the average distance of the electrode pair.

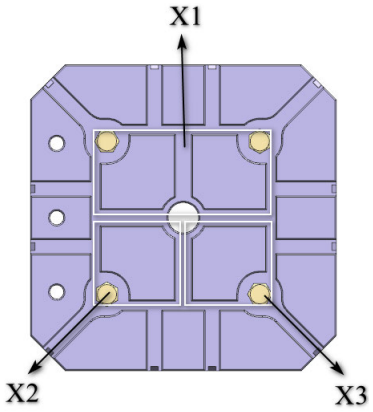

FIGURE 5. Configuration of the electrodes.

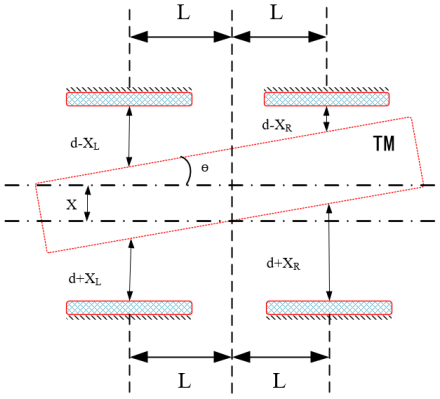

FIGURE 6. Measurements of translation and rotation.

IV. DESIGN OF FRONT-END ELECTRONICS

The FEE is the core component of the inertial sensor. The differential capacitance of the TM and the electrodes is converted into a voltage by the capacitive sensing circuit to achieve accurate detection of the TM position. The feedback voltage is then applied to the electrode through the electrostatic driving circuit. The TM is controlled at the center of the electrode cage.

A. CAPACITIVE SENSING CIRCUIT

The inertial sensor realizes the detection of the TM motion displacement signal by applying a 100 kHz sine wave modulation signal to the TM to form an resonant capacitance (RC) bridge. This bridge includes a differential capacitance comprising of the TM and the electrodes, and a differential transformer. The principle of differential transformer capacitance detection is shown in Figure 7.

In Figure 7, C_1 and C_2 comprise of the TM and the upper and lower electrode plates, respectively. C_{p1} and C_{p2} are parasitic capacitances and resonance tuning capacitors in the circuit, respectively. C_{b1} and C_{b2} are electrostatic feedback-driven filter capacitors. L_1, L_2, and L_s are transformer inductance, and V_f is the electrostatic drive feedback voltage. The high gain of the signal is realized by adjusting

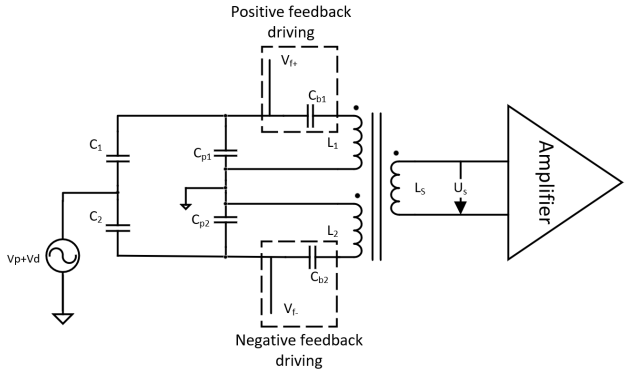

FIGURE 7. Schematic of capacitance detection based on differential transformer.

TABLE 3. Parameters of Front-End Electronics.

Parameters	Value	Unit
Bias Voltage V_p	5	V
Effective value of sensing voltage V_d	4	V
Frequency of sensing voltage f_d	100	kHz
Maximum feedback voltage V_f	± 10	V

the RC bridge working near the resonance point to reduce the noise, and the signal-to-noise ratio of the differential capacitance signal is improved. Thus, the resonant peak of the capacitive inductor and the sine wave modulated signal has the same frequency of 100 kHz. The circuit resistance parameters are shown in Table 3.

As shown in Figures 4 and 7, when the high-frequency injection voltage V_d acts on the TM, the distance between the TM and the two electrodes is equal, which is both d, and the effective area between the capacitor plates is S. The two capacitors with the same capacitance between the electrodes and the TM are recorded as C_1 and C_2:

$$C_1 = C_2 = \frac{\varepsilon_r \varepsilon_0 S}{d} \tag{3}$$

where ε_0 is the vacuum dielectric constant, ε_r is the relative dielectric constant, S is the electrode area, and d is the average distance of electrode pairs. When disturbed by external acceleration, the TM will produce a small displacement Δd, and C_1, C_2 will change accordingly:

$$\Delta C = 2\varepsilon_r \varepsilon_0 S \frac{\Delta d}{d^2} \tag{4}$$

The amount of capacitance change in the upper and lower plates is the amount of position change in the test quality. Owing to the change in capacitance, the voltage generated at the amplifier terminal after passing through the transformer is computed as follows:

$$\begin{aligned} U_s &= \frac{S^2 L \Delta C}{1 + s^2 L(C_1 + C_2 + C_{\mathrm{p1}} + C_{\mathrm{p2}})} V_d \\ &= V_d \frac{S^2 L}{1 + s^2 L C_{\mathrm{eq}}} \Delta C \end{aligned} \tag{5}$$

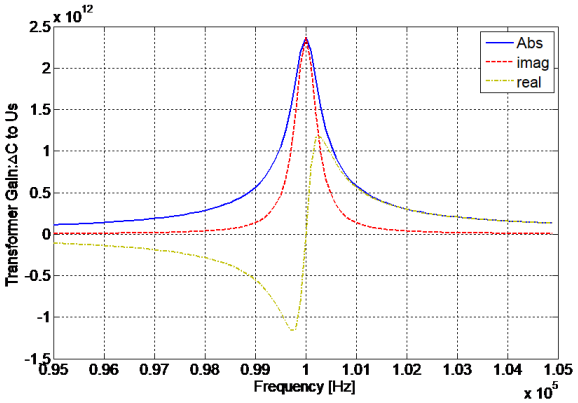

FIGURE 8. Frequency response of differential transformer module.

where $C_{\mathrm{eq}} = 2(C_0 + C_p)$, and C_0 is the capacitance when the TM is in the center of the electrodes. The value of C_0 can be calculated by Equation (3), $C_p = C_{\mathrm{p1}} = C_{\mathrm{p2}}$, and $L_1 = L_2 = L_s = L$. Equation (5) shows that the natural frequency of the transfer function comprising the differential transformer and the capacitor is

$$\omega_0 = \frac{1}{\sqrt{LC_{\mathrm{eq}}}} \tag{6}$$

When the frequency of the input signal is ω_0, the circuit will resonate with the input signal, and the output voltage and impedance both reach maximum values. In the design of this scheme, the resonant frequency is set to 100 kHz by matching the capacitive parameters. According to Equation (5), the frequency response curve of the differential transformer module is shown in Figure 8.

The output voltage U_s of the differential transformer is demodulated by an amplifier, a bandpass filter, and a multiplier. The stimulus signal can be expressed as follows:

$$u_d = V_d \cos\omega_d t \tag{7}$$

where, ω_d is 6.28×10^5 rad/s(that is $f_d = 100$ kHz).

The signal input by the multiplier is an amplitude modulation wave

$$u_{\mathrm{in}} = U_{\mathrm{in}} \cos(\omega t + \alpha)\cos(\omega_d t + \beta) \tag{8}$$

where $U_{\mathrm{in}}\ \cos(\omega t + \alpha)$ is amplitude modulation, ω is $(6.28 \times 10^{-4} - 0.628)$ rad/s [that is, the acceleration measurement passband is $(1 \times 10^{-4} - 0.1)$ Hz], and $\cos(\omega_d t + \beta)$ is the carrier. Then, the output of the multiplier is

$$\begin{aligned} U_{\mathrm{out}} = {} & \frac{U_d U_{\mathrm{in}}}{2} \cos\beta \cos(\omega t + \alpha) \\ & + \frac{U_d U_{\mathrm{in}}}{4} \cos\beta \cos(2\omega_d t + \omega t + \alpha + \beta) \\ & + \frac{U_d U_{\mathrm{in}}}{4} \cos\beta \cos(2\omega_d t - \omega t - \alpha + \beta) \end{aligned} \tag{9}$$

The low-pass filter with a passband far below the detection frequency f_d is used to filter the latter two to obtain the desired signal $\frac{U_d U_{\mathrm{in}}}{2}\ \cos\beta\ \cos(\omega t + \alpha)$. The phase β must be adjusted to zero, because the desired signal contains the factor $\cos\beta$, otherwise, the desired signal will be attenuated.

Finally, the desired signal enters the PID controller, and then a feedback voltage is obtained. This voltage is applied to the electrodes through the electrostatic driving circuit to complete the closed-loop control.

B. ELECTROSTATIC FEEDBACK CONTROL SYSTEM

The TM, electrostatic feedback force, and gas damping effect of the inertial sensor form a classic spring oscillator subsystem. Therefore, the electrostatic system dynamics equation of an inertial sensor can be expressed as follows:

$$m\ddot{x} + c\dot{(x)} + kx = F_{\text{in}} \tag{10}$$

where F_{in} represents external interference into the inertial sensor, m is the quality of the TM, x is the displacement of the TM movement, c is the gas damping coefficient, and k is the stiffness caused by the electrostatic force. When gas damping occurs in the capacitance gap, the damping coefficient of the gas molecules acting on the TM is obtained by gas molecular motion theory [16]

$$c = pS\sqrt{\frac{2M}{\pi RT}} \tag{11}$$

where p is the ambient pressure, M is the molar mass of the gas, $M = 29 \times 10^{-3}$ kg/mol, R is the molar gas constant $R = 8.314$ Nm, and T is the ambient temperature 293 K because the inertial sensor works in a vacuum environment $p = 5 \times 10^{-5}$ Pa. Thus, the gas damping coefficient is small and ignorable.

An electrostatic force expression is established for the unbalanced position to derive the electrostatic force stiffness [17]:

$$F_e = 2\varepsilon_r\varepsilon_0 S\frac{V_pV_rx^2 + (V_p^2 + V_r^2)dx + V_pV_rd^2}{(d^2 - x^2)^2} \tag{12}$$

where V_p represents the preload bias voltage, and V_r represents the feedback voltage of the control output. The square term of x can be neglected because x is considerably smaller than d, and the expression of the electrostatic force is as follows:

$$F_e = 2\varepsilon_r\varepsilon_0 S\frac{(V_p^2 + V_r^2)}{d^3}x + 2\varepsilon_r\varepsilon_0 S\frac{V_pV_r}{d^2} \tag{13}$$

Therefore, the electrostatic force stiffness can be expressed as

$$k_{\text{em}} = 2\varepsilon_r\varepsilon_0 S\frac{(V_p^2 + V_r^2)}{d^3} \tag{14}$$

Combining Equations (10), (13), and (14), the inertial sensor electrostatic kinetic equation is

$$m\ddot{x} = F_{\text{in}} - kx - 2\varepsilon_r\varepsilon_0 S\frac{V_p}{d^2}V_r \tag{15}$$

The Laplace transform of Equation (15) provides the transfer function of the kinetic model:

$$X(s) = \frac{F_{\text{in}}HV_r}{ms^2 - k_{\text{em}}} \tag{16}$$

where $H = \frac{2\varepsilon_r\varepsilon_0 SV_p}{d^2}$ is the scale factor for the system.

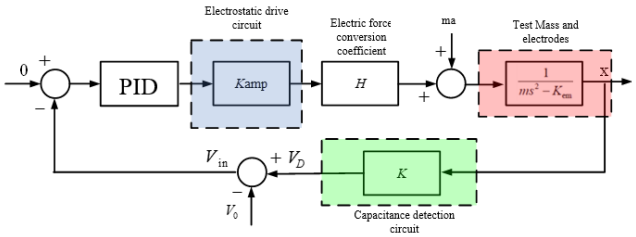

FIGURE 9. Block diagram of closed-loop control of electrostatic levitation inertial sensor.

Figure 9 shows a block diagram of the closed-loop control of an electrostatic levitation inertial sensor containing a PID controller. The role of the PID controller is to provide resistance and improve measurement linearity. The transfer function can be written as follows:

$$C(s) = k_p + \frac{k_i}{s} + k_d s \tag{17}$$

where k_p, k_i, and k_d are the proportional, integral, and differential coefficients of the PID controller, respectively. In Figure 9, K_{amp} represents the gain of the electrostatic drive circuit, H is the conversion coefficient from voltage to force, K denotes the gain of the capacitive sensing circuit and the red square is the kinetic model of the sensitive structure. The above-mentioned modules linked together form a negative feedback closed-loop control system.

When the transfer function of the PID controller $C(s)$ and the electrostatic driving system $X(s)$ is obtained, the closed-loop transfer function of the electrostatic levitation inertial sensor can be expressed as follows:

$$\begin{aligned} G(s) &= \frac{K_{\text{amp}}X(s)C(s)}{1 + K_{\text{amp}}X(s)C(s)} \\ &= \frac{K_{\text{amp}}HKk_ds^2 + K_{\text{amp}}HKk_ps + K_{\text{amp}}HKk_i}{ms^3 + K_{\text{amp}}HKk_ds^2 + (K_{\text{amp}}HKk_p - K_{\text{em}})s + K_{\text{amp}}HKk_i} \end{aligned} \tag{18}$$

where $G(s)$ is the closed-loop transfer function of the control system, and K_{amp} is the gain of the capacitance detection circuit.

The acceleration measurement frequency band is from 0.1 mHz to 1 Hz. Hence the selection of PID parameters should ensure that the closed-loop bandwidth of the system is larger than 1 Hz, and away from the system resonance frequency(approximately 2 Hz). The PID parameters can be selected to obtain closed-loop bandwidth around 20 Hz, $k_p = 2$, $k_i = 12.89$, and $k_d = 0.09$. Taking the X1 axis as an example, the sensitive structural, the FEE and PID parameters are integrated into Equation (18). The actual closed-loop transfer function of the X1 axis is obtained, as shown in Equation (19). The closed-loop frequency response curves of the X1 axis are also obtained (Figure 10).

$$G_{a-X1}(s) = \frac{30s^2 + 119.5s + 142.7}{0.8372s^3 + 29.99s^2 + 115.8s + 142.7} \tag{19}$$

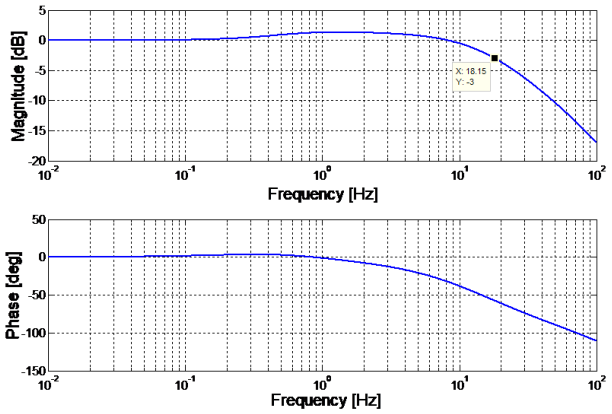

FIGURE 10. Frequency response curve of inertial sensor X1 axis closed-loop system.

Based on the definition of −3 dB bandwidth, the upper limit of the measurement band of the X1 axis is 18.15 Hz. The value can meet the requirements of the 1 Hz measurement band specified by the technical requirements.

V. EXPERIMENTS

A. EXPERIMENTAL SETUP

As shown in Figure 11, a set of experimental platforms for suspension wire torsion pendulum was built to test the performance of the FEE system of the inertial sensor developed in this study. The three-degree-of-freedom closed-loop control stability, range, electricity force conversion factor, and closed-loop acceleration resolution of the FEE system were tested. The experiments were conducted in Changchun, Jilin Province, China on July 2019. The existing conditions were used to place the suspension wire torsion pendulum platform on the vibration isolation marble platform to overcome the effect of ground environment vibration. The laboratory environment can be cleaned up to 1000 levels, and the temperature fluctuation range is ±0.02 °C. The FEE and sensitive structure were connected by a coaxial cable, and the electrical box and the sensitive structure were common grounded.

B. EXPERIMENT RESULTS

The sensitive structure of the inertial sensor is mounted on the precision level adjustment test bench, and the experimental bench uses three orthogonally mounted precision screw adjustment columns to achieve orthogonal adjustment of the horizontal level of the water platform. When the platform is horizontal, the FEE closed-loop correction is turned on. The TM is stably controlled at the center of the two electrode plates. External interference is applied to the TM in the closed-loop process to test the stability. The experimental results show that TM can achieve three-degree-of-freedom stability control. The LabVIEW development interface display software is used, and the control result is shown in Figure 12.

The sensitive structure of the inertial sensor is mounted on the precision level adjustment test bench to calibrate the range and electric force conversion coefficient of the inertial sensor on the ground, the tilting table angle is adjusted by three height adjustments, and the oblique angle is read by level to obtain gravity. The component is used to calibrate the inertial sensor range and the electric force conversion coefficient statically on ground conditions. Figure 13 shows a schematic of the calibration principle, and the calibration results are shown in Figure 14.

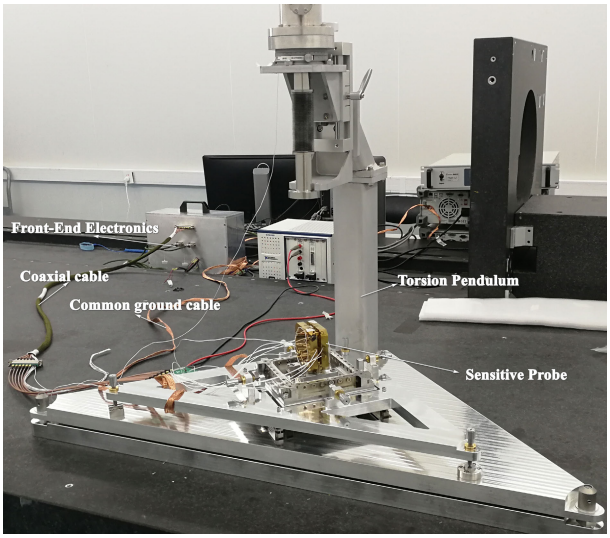

FIGURE 11. Suspension wire torsion pendulum experimental platform.

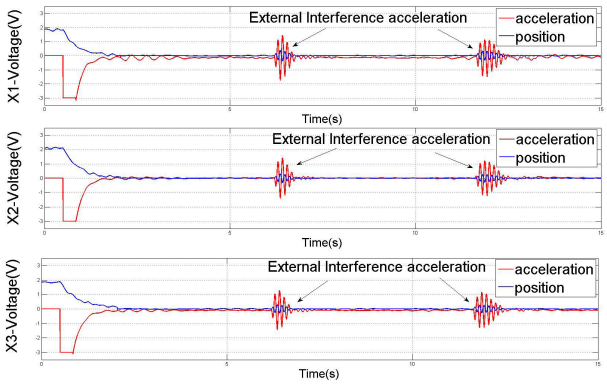

FIGURE 12. LabVIEW interface of three-degree-of-freedom control performance.

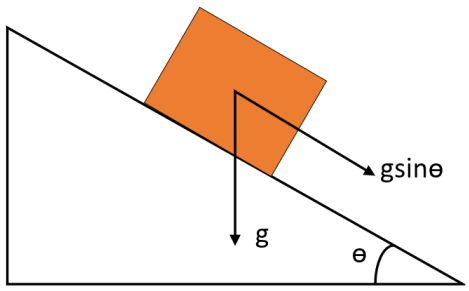

FIGURE 13. Schematic of the calibration principle of the range and electric-force conversion coefficient.

TABLE 4. Results of electrode asymmetric noise.

	Average area (mm^2)	Symmetry deviation Δ	Electrode Distance (μm)	Bias voltage noise ($V/Hz^{1/2}$)	Excitation signal noise($V/Hz^{1/2}$)	Result ($m/s^2/Hz^{1/2}$)
X1	478.46	2.95×10^{-3}	120	1×10^{-5}	1×10^{-5}	4.6×10^{-12}
X2	239.73	8.26×10^{-4}	120	1×10^{-5}	1×10^{-5}	1.3×10^{-12}
X3	239.74	6.07×10^{-4}	120	1×10^{-5}	1×10^{-5}	9.2×10^{-13}

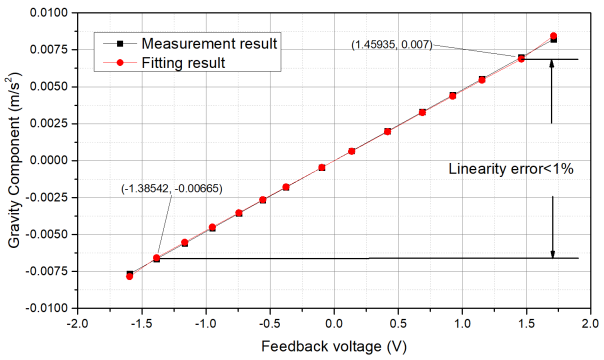

FIGURE 14. Range and electric-force conversion coefficient calibration curve.

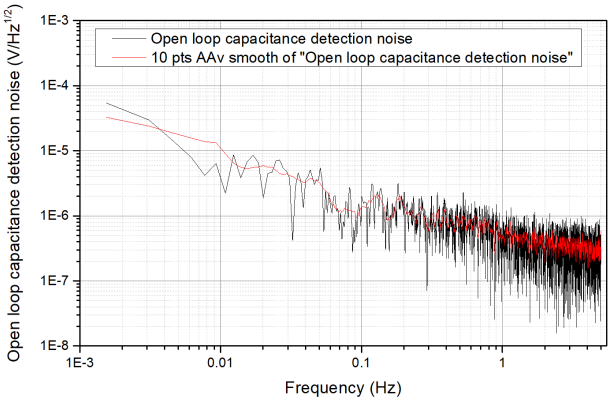

FIGURE 15. Noise floor power spectrum of open-loop capacitance detection circuit.

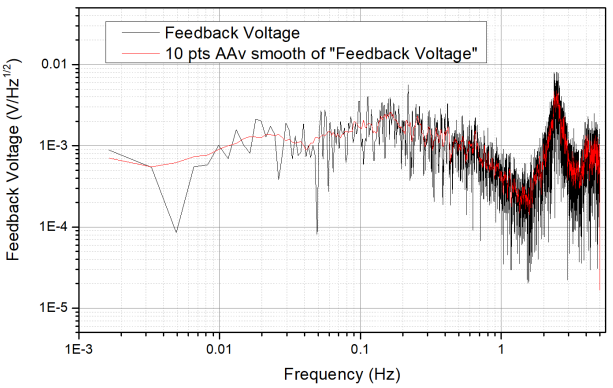

FIGURE 16. Power spectrum of closed loop feedback driving voltage.

In the calibrated range, a linear interval with less than 1% linearity is selected as the acceleration measurement range. As shown in Figure 13, the FEE range designed in this paper is -6.7×10^{-3} m/s^2 to 7.0×10^{-3} m/s^2. By fitting the linear region, the electric force conversion coefficient is 4.8×10^{-3} m/s^2/V.

The evaluation of the acceleration resolution index of the inertial sensor is obtained by testing and noise synthesis of various noise factors affecting the measurement, including external noise, such as sensitive structure machining orthogonality, circuit noise, temperature fluctuation, gas damping, and environmental vibration. The total noise is obtained for the aforementioned main noise test and estimation. The calculation Equation is as follows:

$$a_{\text{total}} = \sqrt{a_1^2 + a_2^2 + a_3^2 + \cdots} \tag{20}$$

For sensitive structure defects, the defects caused by electrode orthogonality and electrode area symmetry are mainly analyzed. Based on the "Machining Inspection Report," the mutual parallelism and verticality of the four sides of the test mass are 3 μm, and the coupling coefficient between the axes can be converted to 1.5×10^{-4} based on the size of the sensitive structure. The coupling acceleration between the axes affects the order of 10^{-10} m/s^2 because the acceleration of the non-conservative force received by the inertial sensor does not exceed 1×10^{-6} m/s^2. The asymmetry influence of the electrode area can be calculated based on the sensor electrode and circuit design parameters, and the calculation Equation is

$$a_{\text{area}} = \frac{2\varepsilon_r \varepsilon_0 \Delta S}{md^2} \left(V_p \tilde{V}_p + V_d \tilde{V}_d \right) \tag{21}$$

where Δ is the asymmetry of the representative area, V_p is the bias voltage fluctuation, and V_d is the amplitude fluctuation of the excitation signal. For the 5 V voltage, the fluctuation of the octave and half multi-meter is within 50 μV, and the power spectrum is analyzed based on 1×10^{-5} V/Hz$^{1/2}$. Taking the sensitive structure and circuit parameters into Equation (21), the acceleration noise caused by the asymmetry of the electrodes is below the order of 10^{-12} m/s^2, and the calculation results are shown in Table 4.

The noise caused by circuit and environmental vibration is evaluated by measuring the noise floor of the capacitance detection circuit under the open-loop condition and the acceleration feedback voltage fluctuation under the closed-loop condition. The power spectrum curve of the capacitance detection under the open-loop condition is shown in Figure 15. The power spectrum of the closed-loop acceleration feedback voltage fluctuation is shown in Figure 16.

As shown in Figure 15, the noise power spectrum of the capacitance detection circuit is below 2×10^{-5} V/Hz$^{1/2}$,

TABLE 5. Total noise of the inertial sensor (unit: m/s^2/Hz$^{1/2}$).

		Sensitive structure defect		Circuit and environment noise		Gas and temperature noise		Total noise
		Electrode orthogonality	Electrode asymmetric	Circuit noise	Environmental vibration	Fluctuation noise	Gradient noise	
X	X1	1×10^{-10}	4.6×10^{-12}	3.4×10^{-9}	9.6×10^{-6}	2.3×10^{-11}	3.6×10^{-12}	9.6×10^{-6}
	X2	1×10^{-10}	1.3×10^{-12}	3.4×10^{-9}	9.6×10^{-6}	2.3×10^{-11}	3.6×10^{-12}	
	X3	1×10^{-10}	9.2×10^{-13}	3.4×10^{-9}	9.6×10^{-6}	2.3×10^{-11}	3.6×10^{-12}	

and the voltage is converted into position measurement noise of 7.2×10^{-11} m/Hz$^{1/2}$. The position measurement noise is multiplied by the stiffness to obtain an acceleration resolution of 3.4×10^{-9} m/s^2/Hz$^{1/2}$. As shown in Figure 16, the power spectrum of the acceleration feedback voltage is below 2×10^{-5} V/Hz$^{1/2}$, and the voltage is multiplied by the power conversion coefficient to obtain the combined effect of the drive circuit and the environmental fluctuation noise of 9.6×10^{-6} m/s^2/Hz$^{1/2}$.

The acceleration noise caused by the effect of the radiometer due to the residual gas and temperature noise inside the sensitive structure is

$$a_{\mathrm{rd}} \cong \frac{PS}{4Tm}\breve{T} \tag{22}$$

where $\breve{T}$ is the temperature fluctuation, T is the ambient temperature, P is the gaseous pressure around the TM, m is the TM mass, and S is the area of the electrode. The experimental environment of this project is characterized by 0.02 K temperature fluctuation. The temperature change will be slow and the change range will be small after passing through the vacuum chamber to the sensitive structure. Meanwhile, 0.02 K/Hz$^{1/2}$ is considered based on the temperature change of the measurement band within the sensitive structure. The degree of vacuum inside the sensitive structure is 1×10^{-4} Pa. Based on Equation (22), the acceleration noise caused by the radiometer effect is 2.3×10^{-11} m/s^2/Hz$^{1/2}$. Owing to the temperature gradient noise observed around the test mass, thermal radiation pressure noise is also caused by the mass. Theoretical analysis shows that the acceleration noise caused by the thermal radiation pressure effect is

$$a_{\mathrm{trip}} = \frac{8\sigma ST^3}{3cm}\breve{T} \tag{23}$$

where σ is the Stephen-Boltzmann constant, $\sigma = 5.67 \times 10^{-8}$ W/(m$^2 \cdot$K^4); and c is the speed of light, $c = 2.9979 \times 10^8$ m/s. Bringing the parameters into Equation (23) results in an acceleration noise of 3.6×10^{-12} m/s^2/Hz$^{1/2}$ due to the temperature gradient. Based on Equation (20), the above estimation and test results are summarized to obtain the total acceleration noise as shown in Table 5.

Table 5 shows that environmental vibration is the main influencing factor of the noise resolution of inertial sensors. On ground conditions, this noise can only be reduced in a cave or an underground environment. If no such noise is present in the space environment, then the total acceleration resolution is recalculated to be 3.4×10^{-9} m/s^2/Hz$^{1/2}$. However, six orders of magnitude difference remain between the indicator of the Taiji Program 10^{-15} m/s^2/Hz$^{1/2}$ due to other aspects, such as machining, temperature fluctuations, and gas damping. Regarding the FEE system, the electrode spacing is increased to 4 mm, and the test quality is increased to 2 kg using high-density materials. The acceleration noise caused by the circuit noise of the FEE system is calculated to be approximately 3.3×10^{-15} m/s^2/Hz$^{1/2}$, which meets the Taiji Program requirements.

VI. CONCLUSION AND OUTLOOK

In this paper, the composition, working principle, and sensitive structure parameters of the inertial sensor FEE system are provided. The electrostatic control system model is derived, and the three-degree-of-freedom stability control is realized. The FEE range and electric force conversion coefficient test are completed. The range of the system is -6.7×10^{-3} m/s^2 to 7.0×10^{-3} m/s^2, and the electric force conversion coefficient is 4.8×10^{-3} m/s^2/V. Finally, the current acceleration noise results of inertial sensors are given. The results show that under current ground conditions, the measured acceleration resolution is only 9.60×10^{-6} m/s^2 due to environmental vibration. If the ground wants to measure high indicators, then a cave or an underground laboratory must be established to suppress the interference of low-frequency noise on the ground. For this system, if the ambient vibration is not considered, then the total acceleration resolution can reach 3.4×10^{-9} m/s^2/Hz$^{1/2}$. At this time, the circuit noise is the main influencing factor, which is mainly related to the sensitive structure parameters. When increased to 4 mm, the TM weight increased to 2 kg, the calculation shows that the FEE system circuit noise caused by the acceleration resolution is approximately 3.3×10^{-15} m/s^2/Hz$^{1/2}$, meeting the Taiji Program requirements.

This paper verifies the feasibility of the FEE system and obtains considerable valuable experience and experimental data. The present work also provides clear ideas for the optimization design of the FEE and lays a solid foundation for the implementation of the future Taiji Program. Simultaneously, a considerable amount of research and experimental verification work must be conducted in mechanical processing, temperature control, ground experimental conditions, and noise source analysis to meet the needs of future space gravitational wave detection.

REFERENCES

[1] B. P. Abbott, "Observation of gravitational waves from a binary black hole merger," *Phys. Rev. Lett.*, vol. 116, no. 6, pp. 1–16, Feb. 2016, doi: 10.1103/physrevlett.116.061102.

[2] W. Haiming, "Humans first detected the gravitational waves generated by the twin-neutron star merger event," *Chin. J. Space Sci.*, vol. 38, no. 1, p. 1, Jan. 2018.

[3] A. Perret, "STAR-The accelerometric system to measure non-gravitational forces on the CHAMP S/C," in *Proc. 49th Int. Astronautically Congr.*, Melbourne, Australia, 1998, pp. 1–6.
[4] A. Bemard and P. Touboul, "The GRADIO accelerometer: Design and development status," in *Proc. Workshop Solid-Earth Mission Aristoteles*, Anacapri, Italy, 1991, pp. 61–67.
[5] P. Touboul and B. Foulon, "ASTRE accelerometer: Verification tests drop tower Bremen," in *Proc. Drop Tower Days Bremen*, Berlin, Germany, 1996, pp. 1–10.
[6] P. Touboul, B. Foulon, and G. M. Le Clerc, "STAR-The accelerometer of geodesic mission CHAMP," in *Proc. 49th Int. Astron. Congr.*, Melbourne, Australia, 1998, pp. 1–7.
[7] M. Armano, H. Audley, J. Baird, P. Binetruy, M. Born, D. Bortoluzzi, E. Castelli, A. Cavalleri, A. Cesarini, and A. M. Cruise, "Beyond the required LISA free-fall performance: New LISA pathfinder results down to 20 *mu*Hz," *Phys. Rev. Lett.*, vol. 120, no. 6, Feb. 2018, Art. no. 061101, doi: 10.1103/PhysRevLett.120.061101.
[8] M. Armano, H. Audley, and G. Auger, "Sub-Femto-g free fall for space-based gravitational wave observatories: LISA pathfinder results," *Phys Rev Lett*, vol. 116, no. 23, pp. 1–10, Jun. 2016, doi: 10.1103/PhysRevLett.116.231101.
[9] H. B. Tu, Y. Z. Bai, Z. B. Zhou, and J. Luo, "Electrostatic-control performance measurement of the inertial sensor with a torsion pendulum," in *Proc. J. Phys., Conf.*, Barcelona, Spain, 2009, pp. 1–6.
[10] W. Tian, S. C. Wu, Z. B. Zhou, S. B. Qu, Y. Z. Bai, and J. Luo, "High resolution space quartz-flexure accelerometer based on capacitive sensing and electrostatic control technology," *Rev. Sci. Instrum.*, vol. 83, no. 9, pp. 1–6, Sep. 2012, doi: 10.1063/1.4749845.
[11] Y.-Z. Bai, Z.-B. Zhou, H.-B. Tu, S.-C. Wu, L. Cai, L. Liu, and J. Luo, "Capacitive position measurement for high-precision space inertial sensor. Front," *Phys. China*, vol. 4, no. 2, pp. 205–208, Feb. 2009, doi: 10.1007/s11467-009-0019-5.
[12] S. Gao, Y. Wang, and Y. Li, "The design of transformer bridge on capacitance detection circuit of electrostatic levitation accelerometer," *Vacuum Cryogenics*, vol. 23, no. 5, pp. 297–300, Oct. 2017, doi: 10.3969/j.issn.1006-7086.2017.05.009.
[13] Z. Xiaoqing, L. Cunhui, W. Zuolei, and M. Jian, "Prospections and issues of electrostatically suspended accelerometer in application to satellite navigation," *SPACE Electron. Technol.*, vol. 1, no. 1, pp. 37–41, Jan. 2018, doi: 10.3969/j.issn.1674-7135.2018.01.007.
[14] D. Cyranoski, "Chinese gravitational-wave hunt hits crunch time," *Nature*, vol. 531, no. 10, pp. 150–151, Mar. 2016, doi: 10.1038/531150a.
[15] H.-S. Liu, Y.-H. Dong, R.-H. Gao, Z.-R. Luo, and G. Jin, "Principle demonstration of the phase locking based on the electro-optic modulator for Taiji space gravitational wave detection pathfinder mission," *Proc. SPIE, Opt. Eng.*, vol. 57, no. 5, pp. 1–6, May 2018, doi: 10.1117/1.OE.57.5.054113.
[16] T. Furong and X. Datong, "Mechanics principle and damping design of a six-axial accelerometer," *J. Sens. Technol.*, vol. 4, no. 1, pp. 287–292, Dec. 2012, doi: 10.3969/j.issn.1004-1699.
[17] F. Da, L. Minjie, L. Yunfeng, Z. Changde, and D. Jingxin, "Servo loop design of capacitive MEMS accelerometer under high preload voltage," in *Proc. Chin. Control Decision Conf.*, Mianyang, China, May 2011, pp. 1341–1344.

YUKUN WANG was born in Hailaer, Hulunbeier, Inner Mongolia, China, in 1988. He received the B.S. and M.S. degrees in control science and engineering from Beihang University, in 2010 and 2013, respectively, and the Ph.D. degree in optical engineering from the University of Chinese Academy of Sciences, Beijing, China, in 2019. From 2013 to 2019, he was a Research Assistant with the State Key Laboratory of Applied Optics, Changchun Institute of Optics, Fine Mechanics and Physics, Chinese Academy of Sciences. His research interests include control system modeling and design, and electronics system design and application.

KEQI QI was born in Inner Mongolia, China, in 1985. He received the B.S. and M.S. degrees in mechanical engineering from Jilin University, in 2007 and 2009, respectively. From 2009 to 2019, he was a Research Assistant with the State Key Laboratory of Applied Optics, Changchun Institute of Optics, Fine Mechanics and Physics, Chinese Academy of Sciences.

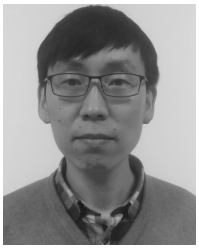

SHAOXIN WANG was born in Inner Mongolia, China, in 1985. He received the B.S. and M.S. degrees in mechanical engineering from Zhejiang University, in 2010 and 2013, respectively. From 2013 to 2019, he was a Research Assistant with the State Key Laboratory of Applied Optics, Changchun Institute of Optics, Fine Mechanics and Physics, Chinese Academy of Sciences.

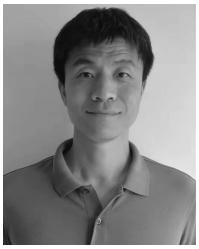

WEI LI was born in Changchun, Jilin, China, in 1980. He received the B.S. degree in electronic science and technology from Jilin University, in 2003, and the M.S. degree in signal and information processing from the Xi'an Institute of Optics and Precision Mechanics, CAS, in 2007. From 2014 to 2019, he was an Associate Professor with the Changchun Institute of Optics, Fine Mechanics and Physics, Chinese Academy of Sciences. His research interest includes space camera system design and application.

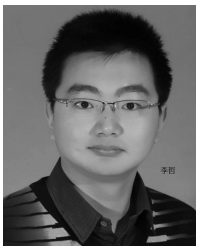

ZHE LI was born in Qiqihar, Heilongjiang, China, in 1984. He received the B.S. degree in electronical information science and technology and the M.S. degree in optics from Xidian University, in 2007 and 2010, respectively. From 2010 to 2019, he was a Research Assistant with the Changchun Institute of Optics, Fine Mechanics and Physics, Chinese Academy of Sciences. His research interest includes electronics system design and application.

ZHI WANG received the B.S. and M.Sc. degrees in mechanical engineering from the Changchun University of Science and Technology, in 1985 and 1988, respectively, and the Ph.D. degree in optical engineering from CIOMP, in 1998. He is currently the Vice-Director of the State Key Laboratory of Applied Optics, CIOMP, CAS. His research interest includes design and manufacturing of space telescope and interferometric systems.